Nanocrystal Heterostructures of LiCoO2 with Conformal Passivating Shells

SCHOLARONE™
Manuscripts

Journal Name

ARTICLE

Nanocrystal Heterostructures of LiCoO₂ with Conformal Passivating Shells

Bob Jin Kwon, [a] Patrick J. Phillips, [b] Baris Key, [c] Fulya Dogan, [c] John W. Freeland, [d] Chunjoong Kim, [a,e] Robert F. Klie[b] and Jordi Cabana[a]*

Stabilization of electrode-electrolyte interfaces is required to increase the energy stored in battery electrodes. Introducing redox-inactive ions on the electrode surface minimizes deleterious side reactions without affecting the bulk properties. A synthetic challenge exists to grow such layers conformally at each primary particle, to fully passivate interfaces that are buried in the final electrode architecture. The development of methods of sequential colloidal growth of complex oxides and overlayers, enabled by surfactant interactions, would provide novel means to advance toward this goal. Here, nanocrystals composed of LiCoO₂, a commercially relevant material for high energy devices, were grown with a shell enriched in Al^{3+}, deposited conformally through a one-pot colloidal synthetic method. The effect of synthetic conditions on the composition of the Al-rich shell and the corresponding electrochemical performance were investigated. The modified nanocrystals showed enhanced electrochemical properties, while maintaining carrier transport.

Introduction

The market of electrical vehicles has clearly identified the development of Li-ion batteries with higher energy and power density than today as a bottleneck for widespread expansion. In these devices, enhancements in energy density necessarily require improving the performance of electrodes, which contain the active materials.[1,2] Layered oxides are leading candidates for the active material of the positive electrode due to their high capacity and potential of operation, which increase the energy storage. Among them, LiCoO₂, which also offers good electronic conductivity upon cycling, was employed in the first devices brought to the market.[3,4] Despite the move to variants where ions such as Ni replace Co, LiCoO₂ continues to be dominant in several applications, while also epitomizing the fundamental challenges of high energy Li-ion batteries. The high operating potential (> 3.9 V vs Li^+/Li^0) leads to spurious reactions at the electrode-electrolyte interface, which involve decomposition of the electrolyte and dissolution of active ions from the oxide.[5,6] These processes contribute to a rapid

degradation of performance. The challenges are further exaggerated when the size of the primary particles is reduced to the nanoscale, which would promote short diffusion lengths for the charge carriers in the final dense architecture.[7] The concomitant high surface area also accelerates degradation at electrode-electrolyte interfaces,[8] which ultimately limits the applicability of nanomaterials. Careful tailoring of electrode/electrolyte interfaces to suppress unwanted side reactions while promoting electrode operation is an essential strategy to produce energy storage technologies that surpass the current performance.

Since interfacial stability in battery electrodes is linked to the redox activity of transition metal ions at the cathode surface,[9] partially replacing them with inactive ions could improve interfacial stability and capacity retention.[10] Such surface replacement should be in the form of ultra-thin passivation layers to minimize losses in the storage capacity of the bulk.[11,12] Various candidates, such as metal oxides, polymer and carbon have been investigated as possible coating materials on active electrodes, by applying physical vapor deposition, wet-chemical techniques and atomic layer deposition (ALD).[13-15] But these post-synthetic methods are typically applied on aggregated powders or even electrodes, which poses restrictions on the conformality and homogeneity of the protective layers, aggravated by the subsequent anneals to remove residual precursors.[16] The result is a lack of complete control over the physical and chemical features of the passivating layers, which creates inefficiencies in the form of incomplete passivation of buried interfaces and excessive use of inactive materials that reduce the energy density of the cell. Therefore, efforts

[a] Department of Chemistry, University of Illinois at Chicago
Chicago, IL 60607, USA. E-mail: jcabana@uic.edu
[b] Department of Physics, University of Illinois at Chicago
Chicago, IL 60607, USA
[c] Chemical Sciences and Engineering Division, Argonne National Laboratory
Argonne, IL 60439, USA
[d] X-ray Science Division, Advanced Photon Source, Argonne National Laboratory
Argonne, IL 60439, USA
[e] School of Materials Science and Engineering, Chungnam National University
Daejeon, 305-764, Republic of Korea

continue to build multifunctional electrode architectures where passivating layers are present in optimal amounts to promote durability without affecting storage capability.

Ideally, all possible surfaces of active powder should be covered by passivation layers that are controlled in composition, thickness and structure. Advances in nanotechnology methodologies over the past two decades have brought about the ability to manipulate individual, dispersible primary particles to deposit shells of the desired properties, thus building precise heterostructures. The ability to form nanocrystalline heterostructures have been demonstrated in the synthesis of quantum dots,[17] magnetic structures[18] and catalysis,[19] but has yet to be fully exploited in battery applications. The compositional complexity of the oxides of interest, with transition metals in fairly high oxidation states (e.g., Co^{3+}, Mn^{4+}) creates significant challenges with existing recipes based on organic environments that are easily oxidized. Recently, we designed a strategy to produce nanocrystals of spinel-type $Li_{1+x}Mn_{2-x}O_4$ with a 1~2 nm epitaxial shell that was rich in Al^{3+}.[20] The coated electrode materials showed an improved cycling durability while maintaining a stable specific capacity, even when subject to harsh environments, such as high temperature cycling. Given the current move away from spinel oxides as electrodes due to their low storage capability,[21] increasing the value of this strategy of active material protection required demonstrating versatility in other compositional spaces, such as layered transition metal oxides. Here, we advance toward this goal by demonstrating a novel recipe for the synthesis of core-shell (CS) nanocrystals based on $LiCoO_2$, a cathode material that enables Li-ion batteries with higher energy density than $Li_{1+x}Mn_{2-x}O_4$. To control the heterostructures, colloidal chemistry was employed to grow a thin shell rich in Al^{3+} in the same reaction environment where the particles were formed and dispersed, ensuring effective coverage of all surfaces. Post-synthetic annealing was used to produce the final heterostructure and tailor the specific chemistry of the shell. An improved understanding of the chemical identity and specific location of core and shell components was confirmed by a combination of X-ray absorption spectroscopy (XAS), solid state nuclear magnetic resonance (NMR) spectroscopy and scanning transmission electron microscopy (STEM). The CS nanocrystals showed improved electrochemical properties compared to their bare counterparts. The improvements were linked to specific chemical signatures in order to chart the path forward for this synthetic approach.

Experimental

Synthesis

The precursor CoO nanocrystals were prepared by following a colloidal synthetic method. First, 4 mM cobalt (III) acetylacetonate (Product No. 494534, Sigma-Aldrich) was dissolved in a 40 mL of oleylamine (OAm) solution (Product No. O7805, Sigma-Aldrich) at room temperature (RT) under a nitrogen blanket in a Schlenk line. In order to remove water and impurities, the mixture was degassed at 100 °C for 20 minutes

under vacuum. The slurry was then heated at 185 °C and maintained it for 1 hour under strong magnetic stirring in an atmosphere of nitrogen gas. Subsequently the temperature was raised to 220 °C and kept for 30 minutes. Aluminium oxide shells were formed on the surface of CoO by a dropwise addition of 20 ml of OAm solution containing 0.8 mmol of aluminium acetylacetonate (Product No. 208248, Sigma-Aldrich) into the CoO colloidal solution at 220 °C. The solution was further annealed for 20 minutes at 220 °C. The resulting nanocrystals were cooled to room temperature in the form of a brown suspension. To remove the oleylamine residues and unreacted products, the nanoparticles were collected by centrifugation for 5 minutes at 10000 rpm, re-dispersed in 15 ml of hexane and washed with ethanol five times. After washing the particles, the powder was dried overnight at 60 °C. In order to prepare $LiCoO_2$, the nanocrystals were thoroughly mixed with $LiOH \cdot H_2O$ (Product No. 43171, Alfa Aesar) at stoichiometric ratios of Li and Co ions and, calcined at 500 °C for 1 or 30 hours in air. Throughout the paper, Bare and CS-$LiCoO_2$ are used as labels for the products without and with Al shells, respectively. $LiCoO_2$ nanocrystals presenting the low temperature, spinel polymorph were prepared from the same precursors, using a different synthetic protocol. Co_3O_4 was obtained by calcining the CoO precursor at 300 °C for 4 hours, and it was subsequently reacted with LiOH at 300 °C for 72 hours.

Characterization

Powder X-ray diffraction was performed on a Bruker D8 Advance using Cu Kα (λ_{avg} = 1.5418 Å) radiation. Scan rates were 0.04 ° s^{-1} from 15° to 80 ° (2θ). Fitting of the patterns to calculate lattice parameters of the different samples was carried out using GSAS-II. TEM images at low magnification were obtained using a JEM 3010 (JEOL) operated at 300 kV. The images were analysed to extract the distribution of particle size and population of different morphologies, by measuring approximately 300 nanocrystals using ImageJ program. Complementary information was collected using scanning electron microscopy (Hitachi S-3000N) fitted with energy dispersive X-ray spectroscopy. All STEM imaging and EDX spectroscopy was performed on an aberration-corrected JEOL JEM-ARM200CF operated at either 200 or 80 kV. Images were acquired in angle annular dark field (ADF) mode, wherein the resulting image intensity is proportional to Z^2. The ARM200CF is equipped with an Oxford X-Max 100TLE windowless silicon drift EDX detector.

Soft X-ray absorption measurements were carried out at beamline 4-ID-C at Argonne National Laboratory (ANL, Lemont, IL). Data was obtained at a special resolution of ~0.1 eV and collected in at the O K-edge and Co L-edges at room temperature and under ultra-high vacuum conditions (below 10^{-8} Torr). A silicon drift diode detector (Vortex) was used to collect the fluorescence yield (FY) and electron yield (EY) positioned near the sample surface. Contributions from visible light were carefully minimized before the acquisition, and all spectra were normalized by the current from freshly evaporated gold on a fine grid positioned upstream of the main chamber.

Co L- and O K-edge spectra were aligned by the beamline reference and a basic normalization using a linear background and edge normalization was performed using Igor program.

^{7}Li and ^{27}Al MAS NMR spectra were acquired at a magnetic field of 7.02 Tesla (300 MHz) on a Bruker Advance III HD spectrometer operating at a Larmor frequency of 116.64 MHz and 78.20 MHz, respectively. A rotor synchronized echo pulse sequence ($\pi/2$ - τ -π - acq.), where $\tau = 1/\nu_r$ (spinning frequency), was used to acquire the ^{7}Li MAS NMR spectra with a 3.2 mm probe at a spinning speed of 20 kHz. A pulse width of 3.5 µs and a pulse delay of 5 seconds were used. The spectra were referenced to 1M LiCl at 0 ppm. For ^{27}Al MAS NMR experiments, a single pulse sequence was used with a pulse width of 1µs and a pulse delay of 2s. The spectra were referenced to 1M Al(NO$_3$)$_3$ at 0 ppm. All experiments were performed at a constant temperature of 283K.

Electrochemical measurements

The electrochemical properties were measured on composites containing the nanocrystals as working electrodes. Electrode slurries were prepared by mixing nanocrystals, carbon black (Denka), and 6 wt% of a solution of polyvinylidene difluoride (PVDF, Kynar) in N-methylpyrrolidone (NMP, Sigma-Aldrich) in 80:10:10 wt %. Then, the slurry was casted on electrochemical-grade aluminium foil using a doctor blade, and dried under vacuum at 70 °C overnight to evaporate NMP moieties. The loading level in the dry electrodes was around 3.0 mg/cm2. Circular pieces with a diameter of 1/2 inch were punched and assembled in two-electrode coin cells in a glovebox filled with Ar gas (the level of contents of water and oxygen were $\leq$ 0.1 ppm). Three coin cells in each material were prepared to calculate average and standard deviation of capacities of cells. High purity lithium foil (Product No. 10769, Alfa Aesar) and 25 µm-thick polypropylene membrane (Celgard 2400) were the counter/reference electrode and separator, respectively. The electrolyte consisted of 1 M LiPF$_6$ in a 3:7, w/w, mixture of ethylene carbonate (EC) and ethyl methyl carbonate (EMC), produced by BASF. Electrochemical measurements were performed on a Biologic BCS-805 at room temperature. The cut-off potentials were set at always 4.3 and 2.0 V, all potentials in this report being referenced to the Li$^+$/Li^0 couple. The values of specific capacity and coulombic efficiency reported were the result of averaging three different cells to assess reproducibility and error. The rate, C/n, was defined as the current density required to achieve a theoretical capacity of C = 274 mAh/g in n hours. The rate capability measurement was measured by fixing the charge current to C/10 while discharge currents were varied from C/10 to 10 C.

Results and discussion

Colloidal CoO nanocrystals were prepared by thermal decomposition of Co (III) acetylacetonate (4 mmol, 1.42504 g) in oleylamine, which plays a role as surface-stabilizing ligand and high boiling point solvent.[22] The passivating layer on the surface was grown by injecting an oleylamine solution of Al (III) acetylacetonate (0.8 mmol, 0.25945 g) into the colloidal

suspension of CoO at 220 °C. A scheme of the synthetic method is presented in figure S1. X-ray diffraction verified the phase purity and structure of the as-made nanocrystals (Figure S2). Both bare CoO and core-shell (CS) CoO presented a cubic rock-salt structure. (JCPDS card number: 43-1004) To synthesize electrochemically active, Li-containing nanocrystals, the rock-salt oxide precursors were mixed with LiOH and calcined at 500 °C in air. The XRD patterns in Figure 1 matched the layered LiCoO$_2$ structure, qualitatively (JCPDS card number: 01-070-2685). In order to minimize grain growth and core-shell inter-diffusion, a reaction time of 1 hour was used. However, small peaks assigned to a Li$_2$CO$_3$ impurity were observed, especially for CS-LiCoO$_2$-1h. Its presence is likely due to the insufficient length of the thermal treatment to complete the reaction. It is possible that some Co$_3$O$_4$ (JCPDS card number: No. 00-042-1467) was present as well, since it also presents a peak at ~32°, but all other reflections overlap with LiCoO$_2$. In contrast, no significant impurities were observed when the synthetic step was carried out in 30 hours. The diffraction peaks were broad, indicative of small particle sizes, and presented asymmetries, as exemplified in the zoomed view between 36.5 and 38°. The asymmetry was ascribed to the presence of both polymorphs of LiCoO$_2$, layered and spinel, which share diffraction peaks.[23] The electrochemical properties of the spinel polymorph are worse than the layered variant.[24-26] Fits of the XRD patterns assuming a layered orthorhombic structure revealed similar values of the *a* dimension for all samples (Table 1). In the case of the interlayer spacing, defined by *c*, an increase was observed with annealing time, both in the presence and absence of Al. CS-LiCoO$_2$-1h presented the lowest value of all samples, which could be linked to incomplete reactions, and the noticeable presence of Li$_2$CO$_3$. The *c/a* ratios of the samples mirrored the trends in *c*, with the highest values associated with the longest annealing times. The layered structures are defined by *c/a* ratios close to 5.00, with lower ratios being indicative of a cubic spinel polymorph.[27,28] All the *c/a* values further support the presence of the low temperature, spinel polymorph in co-existence with the high temperature, layered form of LiCoO$_2$. Such polymorphism is common at when materials are synthesized at low temperature.[29] The increase in *c/a* with reaction time is indicative of an increase of the ratio of layered polymorph. CS-LiCoO$_2$-1h presented a slightly lower *c/a* than the rest of materials, suggesting a slightly higher ratio of spinel polymorph in this sample. The similarity in cell parameters for LiCoO$_2$-30h and CS-LiCoO$_2$-30h suggest that the introduction of Al^{3+} did not significantly affect the bulk structure of the material, as substitution of Co^{3+} in LiCoO$_2$ by Al^{3+} causes an expansion of the *c* axis.[30]
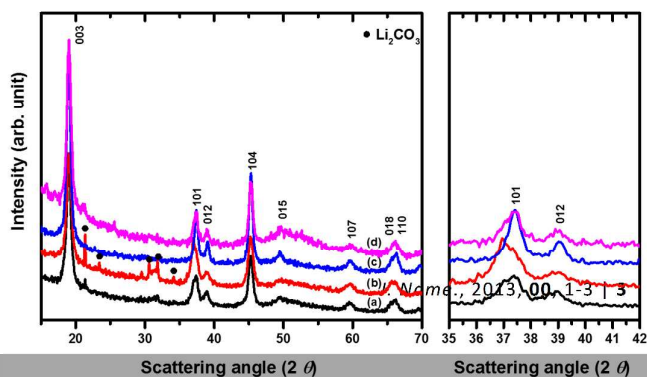
Fig.1 XRD patterns of (a) LiCoO$_2$-1h, (b) CS-LiCoO$_2$-1h, (c) LiCoO$_2$-30h and (d) CS-LiCoO$_2$-30h nanocrystals. Miller indices corresponding to the layered polymorph of LiCoO$_2$ are provided. Solid circled marks indicate Li$_2$CO$_3$ impurities.

	a (Å)	c (Å)	c/a
LiCoO$_2$-1h	2.83	13.96	4.93
LiCoO$_2$-30h	2.82	14.01	4.96
CS-LiCoO$_2$-1h	2.84	13.86	4.87
CS-LiCoO$_2$-30h	2.83	13.99	4.95

Table 1. Unit cell parameters and c/a ratio of all the nanocrystals.

Figures 2a shows the morphology of the CoO precursors, which formed agglomerates of ~70 nm composed of nanocrystals of ~7 nm; all secondary particles presented similar size. It is worth noting that growth of the Al shells was carried out on these uniformly agglomerated particles, while highly dispersed in the reaction solution (Figure S1). Therefore, the shells could not possibly conformally form on the individual 7-nm nanocrystals due to the existence of surfaces buried within the dense 70-nm clusters which would not be reached by the precursor solution. After the reaction with LiOH, the primary particles fused to form objects with a single crystalline appearance, with morphology varying from spherical to faceted, with an appearance of plate (Figures 2c-f and figure S3). [31] Minor grain growth was measured after the reaction at 500 °C, as denoted in the histogram in Figure 2g, which resulted from measuring more than 300 nanocrystals per sample. The ratio of spherical to faceted nanocrystals in bare LiCoO$_2$ was calculated by selecting nine different areas randomly (Figure S3 in the supporting information). The population of each morphology, plotted in figure 2h, indicates an increase in the ratio of platelets with reaction time. In some cases, transition between morphologies was not complete and the particles appeared to present a void in their interior (see Figure
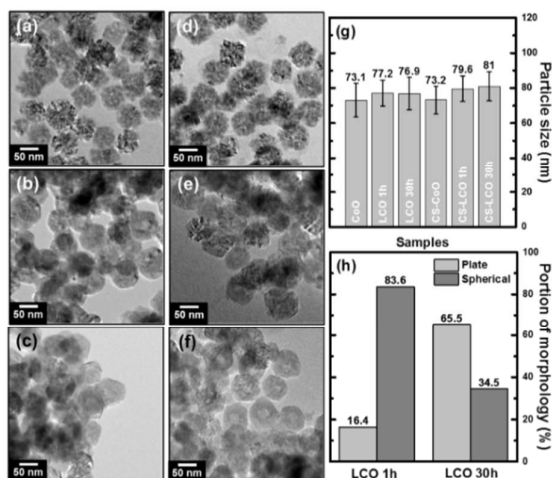

Fig.2 Representative TEM images of (a) CoO precursor, (b) LiCoO$_2$-1h, (c) LiCoO$_2$-30h, (d) CS-CoO, (e) CS-LiCoO$_2$-1h and (f) CS-LiCoO$_2$-30h nanocrystals (All scale bars are same); (g) average particle size of each material with error bars; (h) %

plate vs spherical particles in LiCoO$_2$-1h and LiCoO$_2$-30h nanocrystals.

2f for an example). The same trend can be qualitatively noticed in the samples with shells. This observation is consistent with the increase in the ratio of layered polymorph, which is known to

favor this morphology.[32] Energy dispersive X-ray (EDX) spectroscopy was conducted in a scanning electron microscope (SEM, Figure S4) to measure the ratio of Al/Co in a large portion of the sample. The values were around 0.16 in both core-shell materials. These values correspond to approximately 84 % of Al precursor having reacted to form a coating on the colloidal cobalt oxide particles.
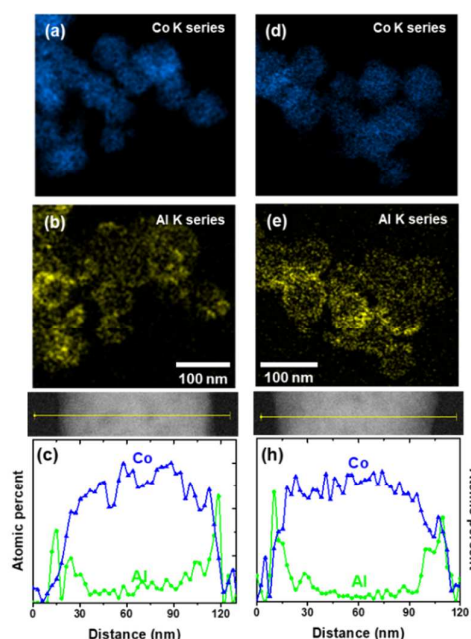

Fig.3 EDX mapping of (a) Co and (b) Al atoms in CS-LiCoO$_2$-1h nanocrystals and corresponding line scans. EDX mapping of (d) Co and (e) Al atom in CS-LiCoO$_2$-30h nanocrystals and (c), (h) corresponding line scans.

The core-shell nature of the nanocrystals was directly confirmed by spatially locating Al and Co atoms via EDX spectroscopy in a high-resolution scanning transmission electron microscope (STEM) operated, at 80 kV primary electron energy. The EDX maps and line scan curves provide information on elemental distribution and concentration throughout the nanocrystals. In all cases, they show a core of Co atoms (Figures 3a and 3d), with Al atoms predominantly located on the surface (Figures 3b and 3e). Additional information was extracted by analyzing line scans conducted along a single particle. Specifically, the concentration of Al in CS-LiCoO$_2$-1h showed a sharp slope upwards approaching the surface region (Figure 3c), while that of CS-LiCoO$_2$-30h reveals a slightly more gradual slope from the surface (Figure

3h). The fact that Co concentrations where higher on the surface after 30 h than 1 h implies the formation of a Al/Co concentration gradient moving from surface to bulk. The measurements indicate that, while the synthetic step at 500°C was not too harsh to wash out the core-shell structure, it did result in a different extent of inter-diffusion, which could affect the electrochemical properties. Atomic resolution STEM imaging (Figure S5) show a nanocrystal consisting of multiple crystalline domains, probably due to intergrowths of spinel and layered phase, without local inhomogenieties on the surface, implying epitaxy with the core.

Solid state NMR experiments were performed to study the lithium and aluminum local environments in the samples prepared. ^7Li MAS NMR data for all four samples show a main isotropic resonance at around -1 ppm, typical of lithium in a diamagnetic local environment, as would be expected by the presence of low spin (t_{2g}^6) Co^{3+} ions in stoichiometric $LiCoO_2$.[33] Both bare $LiCoO_2$ nanocrystals (1 and 30h) had a small shoulder at around 30 ppm suggesting existence of a slight excess of lithium in the structure (Figures 4a and S6).[34] For comparison purposes, the low temperature, spinel polymorph of $LiCoO_2$ was also synthesized and its ^7Li MAS NMR spectrum was collected (Figure 4a). It also presented a resonance close to -1 ppm, again indicative of the presence of Co^{3+}, making it impossible to use NMR to resolve layered from spinel components.
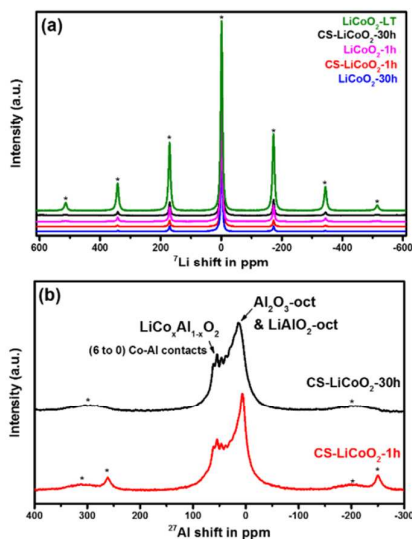

Fig.4 (a) Mass normalized ^7Li MAS NMR spectra of all nanocrystals and (b) ^{27}Al MAS NMR spectra of core shell $LiCoO_2$ with different annealing hours. (Asterisk mark (*) indicates spinning side band)

The nature of the local environments of Al in the core-shell particles was studied with ^{27}Al MAS NMR (Figure 4b). The data for both samples showed at least 6 different aluminium peaks between 20 to 60 ppm, each separated by ~7 ppm. Upon comparison with previous ^{27}Al MAS NMR spectra of $LiAl_xCo_{1-x}O_2$ solid solutions and $LiCoO_2$ coated with Al^{3+} species at high temperatures[34], the signals can be assigned to octahedral Al^{3+}

environments with varying amounts of Co^{3+} in the neighbouring coordination shell. In other words, they are indicative of presence of $LiAl_xCo_{1-x}O_2$ solid solution within the structure. Based on the high resolution elemental maps in Figure 3, this solid solution is most likely located at the interface between core and shell, and reflects the outward gradient in Al/Co ratios. The similar intensities observed in this region for the two core-shell samples reveals that the solid solution formation is driven by annealing temperature but does not depend on annealing time. The major difference between the two samples was found in the region from 0 to 15 ppm, corresponding to octahedral Al^{3+} environments in an oxide without the transition metal.[32] CS-$LiCoO_2$-1h showed a peak around 6 ppm typical of environments in Al_2O_3. This observation suggests the sample also has an oxide layer on the surface, consistent with the very low amount of Co found close to the surface (Figure 3c). This peak shifted to 14 ppm and broadened as the annealing time increased to 30h, ascribed to interfacial phases such as a distorted Al_2O_3 structure and/or $LiAlO_2$, with octahedral Al^{3+}. The subtle but significant difference in Al^{3+} species present in the shell of the nanocrystals was expected to affect the electrochemical properties of the materials, based on previous studies.[35]
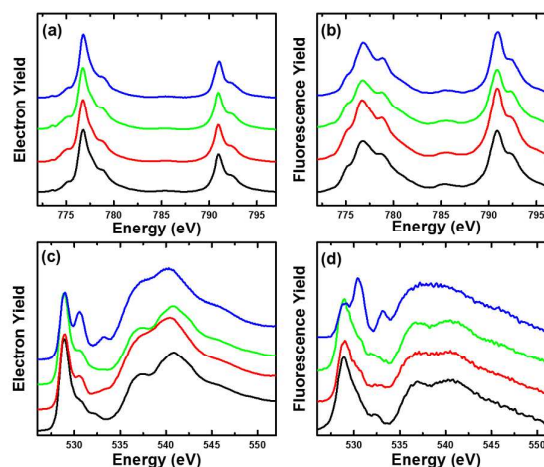

Fig.5 Co $L_{II,III}$-edge and O K-edge XAS, collected in (a, c) TEY and (b, d) TFY mode, of $LiCoO_2$-1h (black), CS-$LiCoO_2$-1h (red), $LiCoO_2$-30h (green), and CS-$LiCoO_2$-30h (blue) nanocrystals.

Soft X-ray absorption spectroscopy (XAS) was performed to examine the electronic environment of Co and O atoms, and the effect of the introduction of Al ions or different annealing time. Spectra were measured using both a total electron yield (TEY) detector, sensitive to the surface, and a fluorescence yield (FY) detector, suitable for characterization of the bulk. Data in FY are affected by absorption of the fluorescent photons by the material, which results in a different, anomalous intensity ratio of the signals compared to TEY. The Co $L_{II, III}$ edge in all cases showed main absorption peaks at ~791 and ~776 eV and weak shoulder peaks at ~792 and ~778 eV, respectively (Figure 5). These signatures are indicative Co^{3+} with a low spin

configuration.[36] The electronic structures of Co were essentially the same in all $LiCoO_2$ materials, which reveals that the redox state of the transition metal was not affected by introducing Al ions on the surface.

The two broad peaks above 535 eV in the O K-edge XAS were assigned to the transition to hybridized states between O 2p and Co 4s/4p and Li 2s bands (Figure 5), as well as mostly ionic O states arising from any aluminum oxides in the shell.[37] The small signal observed at 532.3 eV observed in some samples is consistent with the presence of Li_2CO_3 (C=O bonds) in the samples, as shown by XRD, based on comparisons with the literature.[38] A pre-edge absorption peak at ~527 eV was prominent in all samples. It represents the transition of a 1s electron in oxygen to a 2p level hybridized with the 3d orbitals of Co^{3+} with a low spin electronic configuration (t_{2g}^6, $^1A_{1g}$). The main peak corresponds to a final state of O $1s^1c$ + Co $3d^7$ electronic configuration, where c is the oxygen 1s core hole.[39] No Al-O interactions arise at these energies. In the presence of Al^{3+}-rich shells, the intensity of the peak at 527 eV decreased compared to a new signal at 530.5 eV, accompanied by a very small peak at 534 eV, especially for $CS-LiCoO_2$-30h. The higher energy peak becomes more intense in the bulk (FY) spectrum. This effect cannot be accounted for by spectral distortions inherent to FY detection, suggesting a difference in O electronic states between bulk and surface. The appearance of this peak cannot be due to changes in the oxidation state of Co, since the corresponding Co L-edge spectroscopic results show no changes. It is possible that these states are created by the replacement of some of the Co^{3+} by Al^{3+} in the coordination shell of O^{2-}, which would occur in the $LiCo_{1-x}Al_xO_2$ gradient. It is expected that Al-O interactions will be more ionic than Co-O. Calculations of density of states are required to verify this hypothesis. They were beyond the scope of this study.
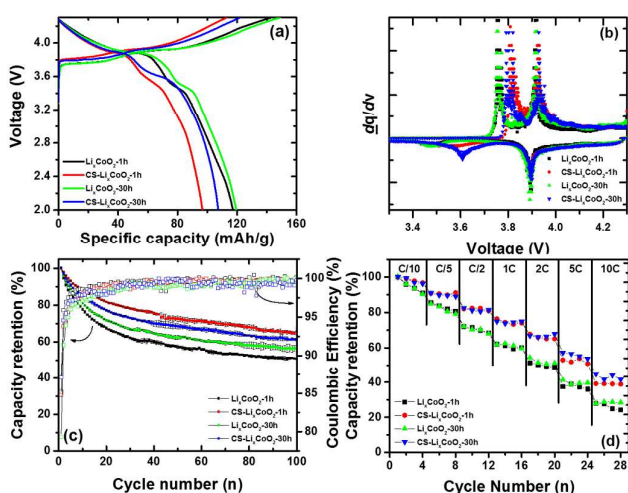

Fig.6 (a) Representative voltage versus specific capacity profiles, (b) corresponding dQ/dV plots, (c) evolution of normalized specific capacity (solid symbol) and coulombic efficiency (open symbol) of bare and core-shell $LiCoO_2$ nanocrystal electrodes when cycled at C/20, and (d) discharging rate capability at room temperature. Errors bars in c result from the averaging of three cells.

The electrochemical performance as electrodes of $CS-LiCoO_2$ nanocrystals with different annealing time were evaluated in Li metal half cells, and compared with bare $LiCoO_2$. Figure 6a shows the voltage versus specific capacity profiles collected in galvanostatic mode during the first cycle at room temperature. Derivative plots, dQ/dV, versus potential (Figure 6b) uncovered two distinct peaks at approximately 3.76 V and 3.92 V during charging, and 3.47 V and 3.89 V during discharging. The two redox potentials were related to the spinel and layered forms of $LiCoO_2$, respectively.[40] A comparison with the electrochemical response of $LT-LiCoO_2$ nanocrystals made at 300 °C (see Supporting Information for details) from the same CoO precursor confirmed this assignment (Figure S7). It is worth noting that the redox potential of the spinel component increased by around 50 mV upon introduction of Al in the sample, whereas the layered component remained constant. The exact origin of this observation is unclear, but could be related to the extensive transformation of spinel domains on the outer domains of the particles to $LiCo_{1-x}Al_xO_2$, which is known to show a shifted potential with respect $LiCoO_2$.[41] The relative concentrations of HT- and LT-phase in all samples were qualitatively established by comparing the values of specific charge capacity above and below 3.9 V during the first charge, as shown Table S1. The comparison suggested a minor increase in relative electroactivity of the spinel phase in $CS-LiCoO_2$-1h compared to the bare counterpart, consistent with the slightly lower c/a cell parameter ratio in the core-shell material observed by XRD. In contrast, the difference in the relative capacity values was not found to be significant for the samples made at 30 h, again in agreement with the XRD analysis above. These observations indicate that the dominant difference between materials was the presence or absence of an Al-rich shell.

The anodic signals were washed out upon subsequent reduction, with this effect being pronounced for the spinel component, and suggesting its early degradation. (Figure S8) Overall, the discharge capacity of both $CS-LiCoO_2$ samples was slightly lower compared to bare $LiCoO_2$, likely due to the presence of electrochemically inactive Al^{3+} species. While bare $LiCoO_2$-1h and -30h had similar first discharge capacities (~120 mAh/g), the specific capacity of $CS-LiCoO_2$-30h (~108 mAh/g) was higher than $CS-LiCoO_2$-1h (~95 mAh/g). It is possible that the kinetics of charge transfer, which promotes utilization, was enhanced by the absence of Li_2CO_3 and a change in the electrical properties of the shell, through the formation of $LiAlO_2$ and an extensive $LiCo_{1-x}Al_xO_2$ gradient, as indicated by TEM-EDX.

Figure 6 (c) presents the capacity retention after 100 cycles in the 4.3-2 V window, for all materials. The values were normalized to the capacity in the first cycle in order to evaluate the effect of the shells, which should be reflected in the retention of electrochemical activity shown in the first cycle. A representation of the data showing the actual capacity values can be found in Figure S9. Three replicas were made for each electrode to ensure the significance of the trends. $CS-LiCoO_2$-1h and 30h showed enhanced cycling durability, with 65.7 %

and 61.3 % retention (63 and 66 mAh/g), respectively, compared to 50.8 % (60 mAh/g) for $LiCoO_2$-1h and 56.4 % (68 mAh/g) for $LiCoO_2$-30h. The improvement brought about by the presence of passivating shells were confirmed in a different electrolyte formulation (Figure S10), involving higher concentrations of $LiPF_6$ and identified by others as suited against high voltage oxide cathodes.[42] In this case, both CS-$LiCoO_2$-1h and 30h showed 80.2 % retention (70 and 83 mAh/g, respectively), compared to 56.3 % (68 mAh/g) for $LiCoO_2$-1h and 60.8 % (79 mAh/g) for $LiCoO_2$-30h, after 50 cycles. The stability of the capacity is still comparably lower than $LiCoO_2$ electrodes suited for Li-ion battery applications.[43] A significant portion of capacity loss is due to the presence of spinel $LiCoO_2$ domains, which are never present in battery-grade electrodes because of the high temperature of synthesis. Indeed, analysis of the voltage profiles (Figures 6b and S8) revealed that losses were more apparent in the process associated with the presence of spinel domains, consistent with its reportedly poor electrochemical performance. This phase degrades rapidly (Figure S8c), with 60% of the capacity lost after just 20 cycles. The loss of activity in the spinel component was much less pronounced in the presence of a shell. Despite the equal or even higher contents of spinel phase that could cause rapid degradation, (Table S1) CS-$LiCoO_2$ showed higher retention of capacity, which hints at the beneficial role of the shell in stabilizing the interface between electrode and electrolyte. The more stable performance of CS-$LiCoO_2$-1h compared to CS-$LiCoO_2$-30h would indicate that the surface chemistry of this phase was more beneficial, likely due to the lower concentration of redox-active Co^{3+}, as indicated by TEM-EDX, since Li_2CO_3 would irreversibly decompose during the first charge. Furthermore, the passivating aluminum oxide layers could act as harvester of HF impurities common in battery electrolytes, thus creating a fluorinated aluminum surface that further protects the surface and slows interfacial loss.[44] The increase in relative stability of the core-shell materials brought about by electrolytes with higher $LiPF_6$ content support the notion that fluorination of the shell is a factor behind their performance. Verification of this hypothesis will be the object of future work. Failure at the bulk was more prominent without the shell, as well; whereas clear redox processes were still discernible after 100 cycles in the core-shell materials, the profiles of bare $LiCoO_2$ were significantly washed out (Figure S11).

The discharge rate capability of CS-$LiCoO_2$ was also more robust than bare counterparts. (Figure 6d). The ratio of capacity at 5 C vs C/10 was 52.5 % and 55.6 % for CS-$LiCoO_2$-1h and 30h, respectively, compared to 37.4 % and 39.8 % for $LiCoO_2$-1h and 30h, respectively. This result implied that charge transfer kinetics is not perturbed by the existence of Al-rich shell, and the lower interfacial degradation maintains it more efficiently.

Conclusions

This study expands our ability to build and manipulate core-shell heterostructures of complex oxides with relevance to energy storage, by demonstrating a colloidal synthetic route toward Al-rich layers grown on individual $LiCoO_2$ nanocrystals. Growth of the heterostructure occurred in a single reaction vessel, followed by modification with Li. The composition of the layer was tailored by thermal annealing, which induces Co/Al inter-diffusion. Detailed insight into the chemistry of core and shell provided by spectroscopy and microscopy suggests a significant level of tunability of the architectures, which provides room to identify critical descriptors to properties. Despite a decrease in the electronic conductivity at the surface, the presence of the shell around individual nanocrystals enhanced the electrochemical performance as Li battery cathodes. The similarity in the pristine bulk structure of all materials strongly suggests a role of the passivation of surface sites in contact with electrolyte on the differences in performance. The compositional versatility of this synthetic procedure is currently being expanded to phases with even more complex compositions, in order to create new avenues for the design of functional electrode materials for Li-ion batteries.

Acknowledgements

References

1   L. Croquennec, M. R. Palacin, *J. Am. Chem. Soc.,* 2015, **137**, 3140-3156.
2   V. Etacheri, R. Marom, R. Elazari, G. Salitra, D. Aurbach, *Energy Environ. Sci.,* 2011, **4**, 3243-3262.
3   W. Lai, C. K. Erdonmez, T. F. Marinis, C. K. Bjune, N. J. Dudney, F. Xu, R. Wartena, Y. Chiang, *Adv. Mater.,* 2010, **22**, E139-144.
4   Y. Nishi, *Chem. Record,* 2001, **1**, 406-413.
5   K. T. Lee, S. Jeong, J. Cho, *Accounts Chem. Res.,* 2013, **46**, 1161-1170.
6   A. Kraytsberg, Y. Ein-Eli, *Adv. Energy Mater.* 2012, **2**, 922-939.
7   P. G. Bruce, B. Scrosati, J. M. Tarascon, *Angew. Chem.-Int. Edit.,* 2008, **47**, 2930-2946.
8   Y. X. Yin, S. Xin, Y. G. Guo, *Part. Part. Syst. Charact.,* 2013, **30**, 737-753.
9   M. Matsui, K. Dokko, K. Kanamura, *J. Power Sources,* 2008, **177**, 184-193.
10 J. Cabana, B. J. Kwon, L. Hu, Acc. Chem. Res. 2018, ASAP.
11 Z. H. Chen, Y. Qin, K. Amine, Y. K. Sun, *J. Mater. Chem.,* 2010, **20**, 7606-7612.

12 I. D. Scott, Y. S. Jung, A. S. Cavanagh, Y. F. An, A. C. Dillon, S. M. George, S. H. Lee, *Nano Lett.,* 2011, **11**, 414-418.
13 L. L. Xiong, Y. L. Xu, T. Tao, X. F. Du, J. B. Li, *J. Mater. Chem.,* 2011, **21**, 4937-4944.
14 H. M. Cho, M. V. Chen, A. C. MacRae, Y. S. Meng, *ACS Appl. Mater. Interfaces*, 2015, **7**, 16231-16239.
15 H. Chen, M. Zhou, T. Wang, F. Li, Y. X. Zhang, *J. Mater. Chem. A,* 2016, **4**, 10786-10793.
16 L. W. Su, Y. Jing, Z. Zhou, *Nanoscale,* 2011, **3**, 3967-3983.
17 X. H. Zhong, R. G. Xie, Y. Zhang, T. Basche, W. Knoll, *Chem. Mat,* 2005, **17**, 4038-4042.
18 T. Yamauchi, Y. Tsukahara, K. Yamada, T. Sakata, Y. Wada, *Chem. Mat,* 2011, **23**, 75-84.
19 R. G. Chaudhuri, S. Paria, *Chem. Rev.,* 2012, **112**, 2373-2433.
20 C. Kim, P. J. Philips, L. Xu, A. Dong, R. Buonsanti, R. F. Klie, J. Cabana, *Chem. Mat,* 2015, **27**, 394-399.
21 M. S. Whittingham, *Chem. Rev.,* 2014, **114**, 11414-11443.
22 S. Mourdikoudis, L. M. Liz-Marzan, *Chem. Mater,* 2013, **25**, 1465-1476.
23 T. Maiyalagan, K. A. Jarvis, S. Therese, P. J. Ferreira, A. Manthiram, *Nat. Commun.,* 2014, **5**, 1-8.
24 S. G. Kang, S. Y. Kang, K. S. Ryu, S. H. Chang, *Solid State Ion.,* 1999, **120**, 155-161.
25 E. I. Santiago, P. R. Bueno, A. V. C. Andrade, C. O. Paiva-Santos, L. O. S. Bulhoes, *J. Power. Sources,* 2004, **125**, 103-113.
26 Y. C. Kan, Y. Hu, Y. Ren, J. Bareno, I. Bloom, Y. K. Sun, K. Amine, Z. H. Chen, *J. Power. Sources,* 2014, **271**, 97-103.
27 R. J. Gummow, M. M. Thackeray, *Mater. Res. Bull.,* 1992, **27**, 327-337.
28 E. Rossen, J. N. Reimers, J. R. Dahn, *Solid State Inoics.* 1993, **62**, 53-60.
29 E. Antolini, *Solid State Ionics,* 2004, **170**, 159-171.
30 Y. Shao-Horn, S. A. Hackney, A. J. Kahaian, M. M. Thackeray, *J. Solid State Chem.,* 2002, **168**, 60-68.
31 J. X. Xu, S. D. Bai, Y. Higuchi, N. Ozawa, K. Sato, T. Hashida, M. Kudo, *J. Mater. Chem. A,* 2015*,* **3***,* 21518-21527.
32 D. Kramer, G. Ceder, *Chem. Mater,* 2009, **21**, 3799-3809.
33 C. P. Grey, N. Dupre, *Chem. Rev.,* 2004, **104**, 4493-4512.
34 M. Murakami, Y. Noda, Y. Koyama, K. Takegoshi, H. Arai, Y. Uchimoto, Z. Ogumi, *J. Phys. Chem. C*, 2014, **118**, 15375-15385.
35 B. Han, T. Paulauskas, B. Key, C. Peebles, J. Park, R. F. Klie, J. T. Vaughey, F. Dogan, *Appl. Mater. Interfaces*, 2017, **9**, 14769–14778.
36 C. H. Chen, B. J. Hwang, C. Y. Chen, S. K. Hu, J. M. Chen, H. S. Sheu, J. F. Lee, *J. Power. Sources*, 2007, **174**, 938-943.
37 W. Hetaba, A. Mogilatenko, W. Neumann, *Micron*, 2010, **41**, 479-483.
38 C. Yogi, D. Takamatsu, K. Yamanaka, H. Arai, Y. Uchimoto, K. Kojima, I. Watanabe, T. Ohta, Z. Ogumi, *J. Power. Sources,* 2014, **248**, 994-999.
39 W. S. Yoon, K. B. Kim, M. G. Kim, M. K. Lee, H. J. shin, J. M. Lee, J. S. Lee, *J. Phys. Chem. B.,* 2002, **106**, 2526-2532.
40 P. R. Bueno, N. C. Presquero, F. F. Ferreira, E. I. Santiago, J. A. Varela, E. Longo, *J. Phys. Chem. C,* 2008, **112**, 14655-14664.
41 G. Ceder, Y. M. Chiang, D. R. Sadoway, M. K. Aydinol, Y. I. Jang, B. Huang, *Nature*, 1998, **392**, 694-696.
42 C. C. Su, M. N. He, C. Peebles, L. Zeng, A. Tornheim, C. Liao, L. Zhang, J. Wang, Y. Wang, Z. C. Zhang, *ACS Appl. Mater. Interfaces*, 2017, **9**, 30686-30695.
43 H. L. Chen, C. P. Grey, *Adv. Mate*r. 2008, **20**, 2206.
44 J. L. Tebbe, A. M. Holder, C. B. Musgrave, *ACS Appl. Mater. Interfaces*, 2015, **7**, 24265-24278.